

THE ENERGY-DEPENDENT X-RAY TIMING CHARACTERISTICS OF THE NARROW LINE
SEYFERT 1 MKN 766A. MARKOWITZ^{1,2}, I. PAPADAKIS³, P. ARÉVALO⁴, T.J. TURNER^{1,5}, L. MILLER⁶, J.N. REEVES^{1,7}¹ X-RAY ASTROPHYSICS LABORATORY, CODE 662, NASA/GODDARD SPACE FLIGHT CENTER,
GREENBELT, MD 20771, USA; AGM@MILKYWAY.GSFC.NASA.GOV² NASA POST-DOC RESEARCH ASSOCIATE³ PHYSICS DEPARTMENT, UNIVERSITY OF CRETE, P.O. BOX 2208, 71003 HERAKLION, GREECE⁴ SCHOOL OF PHYSICS AND ASTRONOMY, UNIVERSITY OF SOUTHAMPTON, SOUTHAMPTON SO17
1BJ, UK⁵ DEPARTMENT OF PHYSICS, UNIVERSITY OF MARYLAND BALTIMORE COUNTY, 1000 HILLTOP
CIRCLE, BALTIMORE, MD 21250, USA⁶ DEPARTMENT OF PHYSICS, UNIVERSITY OF OXFORD, DENYS WILKINSON BUILDING, KEBLE
ROAD, OXFORD OX1 3RH, UK⁷ DEPARTMENT OF PHYSICS AND ASTRONOMY, JOHNS HOPKINS UNIVERSITY, BALTIMORE, MD
21218, USA

ABSTRACT

We present the energy-dependent power spectral density (PSD) and cross-spectral properties of Mkn 766, obtained from combining data obtained during an *XMM-Newton* observation spanning six revolutions in 2005 with data obtained from an *XMM-Newton* long-look in 2001. The PSD shapes and rms-flux relations are found to be consistent between the 2001 and 2005 observations, suggesting the 2005 observation is simply a low-flux extension of the 2001 observation and permitting us to combine the two data sets. The resulting PSD has the highest temporal frequency resolution for any AGN PSD measured to date. Applying a broken power-law model yields break frequencies which increase in temporal frequency with photon energy. Obtaining a good fit when assuming energy-independent break frequencies requires the presence of a Lorentzian at $4.6 \pm 0.4 \times 10^{-4}$ Hz whose strength increases with photon energy, a behavior seen in black hole X-ray binaries. The cross-spectral properties are measured; temporal frequency-dependent soft-to-hard time lags are detected in this object for the first time. Cross-spectral results are consistent with those for other accreting black hole systems. The results are discussed in the context of several variability models, including those based on inwardly-propagating viscosity variations in the accretion disk.

Subject headings: galaxies: active — galaxies: Seyfert — X-rays: galaxies — galaxies: individual (Mkn 766)

1. INTRODUCTION

Seyfert active galactic nuclei (AGNs) and stellar-mass black hole X-ray binary systems (XRBs) both exhibit rapid, aperiodic X-ray variability that likely originates in the innermost regions of these compact accreting objects. The dominant X-ray radiation is generally thought to be inverse Comptonization of soft seed photons by a hot corona (e.g., Shapiro et al. 1976, Sunyaev & Titarchuk 1980), though the exact geometry is uncertain and numerous configurations have been invoked (e.g., Zdziarski et al. 2003). The X-ray variability can be characterized by fluctuation power spectral density functions (PSDs) which reveal the "red-noise" nature of the variability at relatively high temporal frequencies in both AGNs and XRBs. Modeling of the broadband PSDs of XRBs usually utilizes some combination of one, two, or more Lorentzians, which tend to dominate in the so-called low/hard energy spectral state, plus a broadband noise component characterized as $P(f) \propto f^{-1}$, which tends to dominate in the high/soft state (e.g., in Cyg X-1; see Axelsson et al. 2005). Quasi-periodic oscillations, or QPOs, are detected in some XRBs, usually those in the so-called Very High spectral state (e.g., McClintock & Remillard 2006).

Broadband PSDs have also been constructed for AGNs, allowing modeling of the overall PSD shape. Specifically, 'breaks' in the power-law PSD models on time scales of a few days or less have been identified for roughly a dozen AGN (e.g., Uttley, M^cHardy & Papadakis 2002; Markowitz et al. 2003; Vaughan, Fabian & Nandra 2003b, hereafter VFN03; M^cHardy et al. 2004, 2005), with power-law slopes $\lesssim -2$ above the break and ~ -1 below it. No evidence for QPOs has been found in AGN PSDs yet. One reason for this may that the insufficient sampling of the observed AGN light curves so far does not allow one to achieve a high enough temporal frequency resolution (Vaughan & Uttley 2005). Nonetheless, the overall similarity in Seyferts' and XRBs' broadband PSD shapes and scaling of PSD break time scale with black hole mass (e.g., Markowitz et al. 2003, M^cHardy et al. 2004), as well as the presence of a linear relation between flux and absolute rms variability (e.g., Uttley & M^cHardy 2001, Edelson et al. 2002), support the notion of similar X-ray variability mechanisms being present in both classes of accreting compact objects. That is, Seyferts and XRBs may simply be scaled versions of each other in black hole mass and X-ray variability time scale.

Further support for this picture comes from observations of the PSD slope above the break to flatten with increasing energy. Previous studies of both XRBs (e.g., Nowak et al. 1999a, Lin et al. 2000) and Seyferts (Nandra & Papadakis 2001, VFN03, M^cHardy et al. 2004, and Markowitz 2005; see also Leighly 2004) have suggested that the PSD slope flattens as photon energy increases. There has been no evidence yet for break frequency to change significantly with photon energy in either AGN or XRBs during a single observation.

The observed cross-spectral properties, namely the coherence function (Vaughan & Nowak 1997) and time lag spectrum, are also similar between Seyferts and XRBs. The coherence is generally seen to be close to unity over a wide range of temporal frequencies in both AGNs and XRBs, usually dropping significantly below unity at frequencies above the PSD break (e.g., Nowak et al. 1999a, 1999b in XRBs; VFN03, M^cHardy et al. 2004 and Markowitz 2005 in AGN). Relatively harder X-rays are seen to generally lag those at softer X-ray energies, with the lag between bands increasing with increasing energy separation. However, lags are also observed to increase with decreasing temporal frequency (e.g., Miyamoto & Kitamoto 1989, Miyamoto et al. 1991, Nowak et al. 1999a in XRBs), with time lags usually $\lesssim 1 - 10\%$ of the Fourier time scale. In the low-hard state of Cyg X-1, the time lags increase in a step-like fashion (e.g., Nowak 2000), which can be explained if the lag at each step is associated with individual Lorentzian components in the broadband PSD. Obtaining time lags via the cross-spectrum requires extremely high quality data with sufficient sampling and number of points. Results for AGN so far have yielded time lag spectra with many fewer points than in XRBs, but also showing the general increase in time lags as temporal frequency decreases (Papadakis, Nandra & Kazanas 2001, VFN03, M^cHardy et al. 2004, Markowitz 2005, and Arévalo et al. 2006a).

Mkn 766 is a well-studied Narrow-Line Seyfert 1 (NLSy1), and thus belongs to a class of objects in which large-amplitude rapid X-ray variability is commonly observed. Timing properties of Mkn 766 have been studied previously by Vaughan & Fabian (2003; hereafter VF03), who measured the broadband PSD, finding a break from steep PSD power-law slope of $\lesssim -2.5$ to ~ -1 near 5×10^{-4} Hz. VF03 also observed the slope above the break to flatten from ~ -2.7 at soft X-rays to ~ -2.2 at hard X-rays; however, they saw no obvious trends in break frequency with energy. VF03 were the first to measure the coherence in Mkn 766. In addition, Vaughan et al. (2003a) observed the linear rms-flux relation in Mkn 766.

In this paper, we present the timing properties of Mkn 766 using the enormous wealth of data obtained from uninterrupted *XMM-Newton* observations in 2005 and 2001. We find that the variability properties of the source during both observations were identical. We therefore combined the 2001 and 2005 light curves to construct power- and cross-spectra with the highest frequency resolution in log space seen in an AGN PSD so far. The rest of this paper is organized as follows: §2 describes the data reduction. §3 demonstrates similarities in the variability properties of the 2001 and 2005 observations. §4 describes measurement of, and model fits to, the energy-dependent PSD made

from combining all the 2001 and 2005 data. §5 describes the cross-spectral properties. The results are discussed in §6 in the context of phenomenological variability models. Finally, a brief summary is given in §7.

In one of two companion timing papers, Papadakis et al. (in prep.; hereafter Paper II) combine the 2001 and 2005 *XMM-Newton* light curves with long-term light curves obtained from *RXTE* monitoring. That paper concentrates on study of the low-frequency PSD shape of Mkn 766 to probe similarities to the broadband PSD shapes of XRBs. In the other paper, Arévalo et al. (in prep.; Paper III) continue the study of the energy-dependent variability properties via Fourier-resolved spectroscopy.

2. OBSERVATIONS AND DATA REDUCTION

Mkn 766 was observed by *XMM-Newton* on 2005 May 23 – 2005 June 3, over revolutions 999–1004. This paper uses data taken with the European Photon Imaging Camera (EPIC), which consists of one pn CCD back-illuminated array sensitive to 0.15–15 keV photons (Strüder et al. 2001), and two MOS CCD front-illuminated arrays sensitive to 0.15–12 keV photons (MOS1 and MOS2, Turner et al. 2001). Data from the pn were taken in Small Window mode; data from each MOS were taken in Large Window mode. The medium filter was used for all detectors.

Light curves were extracted using SAS version 6.5 using standard extraction procedures. Data were selected using event patterns 0–4 for the pn and 0–12 for each MOS. Hot, flickering or bad pixels were excluded. Source light curves were extracted from circular regions of radius 40"; background light curves were extracted from circles of identical size, centered $\sim 3'$ away from the source. We checked for pile-up; there was no significant pile-up in the pn and at most a few percent pile-up in each MOS.

The 2–12 keV pn light curve was analyzed for background flares; any data where the pn background rate exceeded 0.2 ct s^{-1} were excluded. Most data excluded occurred at the beginnings or ends of revolutions (e.g., the final 18 ksec of revolution 999 data, the final 17 ksec of revolution 1003, and the final 13 ksec of revolution 1004). This screening also introduced a 10 ksec gap into the revolution 1003 light curve. Because such large gaps tend to reduce the statistical significance of variability parameters derived over the full duration, the light curve was split into two smaller light curves, hereafter designated 1003A and 1003B, for a total of seven virtually uninterrupted light curves. All other gaps introduced by background screening were small (< 1 ksec) and in the analyses below, fluxes during gaps were linearly interpolated from adjacent points.

Data were extracted over the 0.2–12 keV (total), 0.2–0.5 keV (soft), 0.5–1.1 keV (medium), and 1.1–12 keV (hard) bands (also referred to as T, S, M and H bands, respectively, below). The S, M and H band limits were chosen such that all three bands had approximately the same count rates. Consequently, the variability due to Poisson noise (see §4 and 5) was roughly the same level, mitigating any effect that the difference in count rates or Poisson noise between bands could have on analysis. Light curves from the three EPIC cameras were summed, using only data taken when all three cameras were in operation simultaneously; this yielded a total exposure time (summed over

all light curves) of 442 ksec. Given the wide bands used here, the differences between pn and MOS response shapes have a negligible effect; the average pn and MOS photon energies for each band differed only by small amounts. In addition, Mkn 766 is a soft-spectrum source, and the inclusion of the MOS data compared to the pn data alone greatly improved signal/noise in the M and H bands. Light curves were binned to 60 s; they are shown in Figure 1. The summed T, S, M and H band light curves have mean count rates (after background subtraction) of 13.44, 4.39, 4.39, and 4.93 ct s⁻¹, respectively. We use these summed light curves in all analyses below except the rms-flux relation and F_{var} spectra, where only pn data are used.

Mkn 766 was also observed during revolution 265 from 2001 May 20 – 2001 May 21. The pn and MOS2 were both in Small Window mode; the MOS1 was in Timing mode and is not considered further. Data were extracted from the pn and MOS2 using the same procedure and bands as for the 2005 data. No significant pile-up was found in the pn or MOS2. This reduction yielded a 107.1 ksec light curve summed over the pn and MOS2. The summed T, S, M and H band light curves have mean count rates (after background subtraction) of 26.85, 9.18, 9.34, and 8.12 ct s⁻¹, respectively. The pn light curve is presented in VF03.

3. BASIC VARIABILITY PROPERTIES

To quantify variability amplitude as a function of energy, we constructed F_{var} spectra for the 2005 observation using the pn data and bin sizes of 6 ksec, and using the formulation of Vaughan et al. (2003a). Figure 2 shows the F_{var} spectrum over the entire observation, and during the lowest- and highest-flux revolutions; the plots confirm relatively high levels of variability, as expected for a NLSy1. The strongest variability amplitudes are found near 1–2 keV in both the 2001 (VF03) and 2005 F_{var} spectra, a result similar to e.g., VFN03 for MCG-6-30-15. The results corroborate the principal component analysis of Miller et al. (2006), who demonstrate that the variability of the continuum component in the soft and hard bands is diluted by the presence of less-variable components, namely the Compton reflection spectrum in the hard band and by the soft excess and narrow emission lines in the soft band.

Compact accreting black holes display “weakly non-stationary” behavior in that the mean and variance both show scatter over time, although both the underlying PSD shape and the expectation value of the fractional variability amplitude $\langle F_{\text{var}} \rangle$ are expected to remain constant in time, e.g., over time scales shorter than decades to centuries in AGN. A constant $\langle F_{\text{var}} \rangle$ in flux is equivalent to the linear rms-flux relation; Vaughan et al. (2003a) previously established the presence of both a linear rms-flux relation and constant $\langle F_{\text{var}} \rangle$ with flux in Mkn 766 using the 2001 data.

We use the enormous wealth of data from the 2005 observation to revisit this issue. The average 0.2–12 keV flux was 3×10^{-11} erg cm⁻² s⁻¹ (e.g., Turner et al. 2006), about half that of the 2001 observation, 6×10^{-11} erg cm⁻² s⁻¹ (e.g., Pounds et al. 2003), allowing us to test if the rms-flux relation has persisted over a four year time scale and can extend to lower fluxes. We measured variability amplitudes in the T-band light curve over short time scales, using only pn light curves to facilitate compar-

ison between 2001 and 2005. We calculated the flux, F_{var} , and the rms amplitude σ_{rms} every 2000 seconds (subtracting off the variance due to Poisson noise). Light curves with ≤ 10 points were discarded. Flux, rms amplitude, and F_{var} points for all seven light curves from 2005 were combined; points were sorted according to flux, and binned in groups of 10. Results are shown in Figure 3. Both observations are consistent with a linear $\langle \sigma_{\text{rms}} \rangle$ -flux relation, as shown in top panel, and with $\langle F_{\text{var}} \rangle$ being constant in flux, as shown in the bottom panel. Moreover, the 2001 and 2005 relations are roughly consistent with each other, indicating that characteristics of the underlying variability process have not significantly changed since 2001, and the 2005 observation is merely a low-flux extension of the 2001 observation. The positive x-intercepts of the best-fit $\langle \sigma_{\text{rms}} \rangle$ -flux relations suggest the presence of a constant component whose magnitude has not changed significantly between the two observations; this qualitatively corroborates the principal component analysis of Miller et al. (2006).

We performed another test for strong non-stationarity using the PSD shapes; as described in the Appendix, the PSD shapes from 2001 and 2005 are consistent with each other. Having established that the variability processes are consistent between the 2001 and 2005 observations, we combine the 2001 and 2005 light curves in all analyses below to maximize the temporal frequency resolution. The difference in mean count rates (e.g., summed over pn + MOS2 in 2001 compared to pn + MOS1 + MOS2 in 2005) is irrelevant since light curves are mean-subtracted and mean-normalized in all analyses below.

Virtually identical results are obtained when using the 2005 data only, though below we present results from the combined 2001 and 2005 binned PSD, which features $\sim 25\%$ higher temporal frequency resolution in log space.

4. THE ENERGY DEPENDENCE OF THE HIGH-FREQUENCY PSD

The high-quality (uninterrupted and highly variable) light curves allows us to create a very high quality PSD for Mkn 766; in particular, the temporal frequency resolution allows very tight constraints on break frequency. §4.1 describes how the PSDs were constructed; §4.2 describes model fits to the PSD shapes.

4.1. PSD Construction

The construction of the PSDs is summarized here; for further details on PSD construction, see e.g., Uttley et al. 2002, Markowitz et al. 2003, VFN03, and references therein. Unlike Paper II, we do not include *RXTE* Proportional Counter Array (PCA) monitoring data, since the PCA bandpass does not go below 2 keV and this paper’s aim is to explore the PSD behavior across as wide an energy range as possible. First, for each of the seven light curves from 2005 and for the 2001 light curve, the mean was subtracted. Periodograms were then calculated separately for each of the eight light curves using a Discrete Fourier Transform (DFT; e.g., Oppenheim & Shafer 1975). The PSD normalization of van der Klis (1997) was used. All periodogram points from the eight light curves were combined and sorted in temporal frequency. Following Padidakis and Lawrence (1993), the periodogram was binned

in log space in groups of 25. This process yielded a PSD for each of the T, S, M and H bands, each with a usable temporal frequency range of $2.57 \times 10^{-5} - 8.27 \times 10^{-3}$ Hz. Power at temporal frequencies above $\sim 3 \times 10^{-3}$ Hz were dominated by the white noise power due to Poisson noise; this observed level of power agreed well with predicted values calculated as $P_{\text{Psn}} = 2(\mu + B)\mu^{-2}$, where μ and B are the exposure-weighted net source and background rates, respectively. The T-band PSD $P(f)$ is plotted in Figure 4a (in $f - P(f)$ space). The S, M, and H-band PSDs are plotted in Figures 5a and 5b (both in $f - f \times P(f)$ space).

4.2. PSD Model Fits

We now discuss model fits to the broadband PSD shape. Monte Carlo simulations (e.g., Uttley et al. 2002) are frequently employed in PSD measurement when it is necessary to account for PSD measurement distortion effects and to assign errors to poorly-sampled PSD points. However, for the present PSDs, we expect no aliasing since each of the individual light curves were continuously sampled and large gaps were excluded. The effects of red noise leak from temporal frequencies lower than those sampled here are likely small given the measured PSD shape, and at any rate are assumed not to vary significantly with photon energy. Finally, because each PSD bin contains a sufficient number of unbinned periodogram points (25), PSD errors are normal, removing the need for Monte Carlo simulations to determine PSD errors. All model fitting was done in log space. We used least-squares fitting (e.g., Bevington 1969) to determine the PSD amplitude. Errors below correspond to $\Delta\chi^2 = 2.71$.

4.2.1. Unbroken and Broken Power-law Model Fits

We first fit an unbroken power-law of the form $P(f) = A(f/f_0)^{-\beta} + P_{\text{Psn}}$ where the normalization A is the PSD amplitude at the (arbitrary) frequency f_0 . β is the power law slope; e.g., positive values of β denote red-noise PSD slopes. P_{Psn} is the constant level of power due to Poisson noise, kept fixed in all fits at the predicted values, which are calculated to be 0.16, 0.44, 0.48 and 0.44 Hz $^{-1}$ for the T, S, M and H bands, respectively. P_{Psn} was added to the model as opposed to being subtracted from the data, to avoid the possibility of obtaining unphysical negative powers. Values of β were tested in increments of 0.02. Results for the best-fit model are listed in Table 1; residuals to the fits are shown in Figures 4b (T-band) and 5c (S, M, and H bands). As per VF03, the fits are quite poor and signal the need for a break in the PSD model.

We next tried fitting broken power-law models. In AGN PSDs, it has not always been clear if the breaks are sharp or instead follow a slow bend. We fit a sharply-broken power-law model of the form

$$P(f) = \begin{cases} A(f/f_b)^{-\gamma} + P_{\text{Psn}}, & f \leq f_b \\ A(f/f_b)^{-\beta} + P_{\text{Psn}}, & f > f_b \end{cases}$$

Here, γ and β are the power-law slopes below and above the break frequency f_b ; A is the PSD amplitude at f_b . We also tested a slowly-bending power-law model,

$$P(f) = Af^{-\gamma}(1 + (f/f_b)^{\beta-\gamma}) + P_{\text{Psn}}$$

Here, γ and β are the power-law slopes far below or above, respectively, the rollover frequency f_b . A is the PSD normalization. Values of $\log(f_b)$ were tested in increments of

0.01; values of β and γ were tested in increments of 0.02. Results for the best-fit models with β , γ , f_b and A free are listed in Table 2; and the residuals are shown in Figures 3c and 3d (T-band) and Figures 5d and 5e (S, M, and H bands).

These fits are significantly better (all $> 4.2\sigma$ confidence in an F-test) compared to the unbroken power-law model fits. Both sharply-broken and slowly-bending model shapes yield similar fits. There is no obvious trend in either β or γ with photon energy in either case. We note that γ is similar to the PSD power-law slope $\lesssim 10^{-3.5}$ Hz obtained from fitting the *XMM-Newton* and long-term *RXTE* data, as shown in Paper II. For either shape, though, f_b for the S band is significantly lower by $\sim 0.2 - 0.5$ in the log (depending on the model used) compared to f_b for the M or H bands.

We explored if it was significant to keep β and γ thawed in the fits. We repeated the fits, with β and γ frozen at the average value of the S, M and H-band fits. Results are listed in Table 2 and the best-fit models are plotted in Figures 5a and 5b. The sum of S, M and H χ^2/dof (degrees of freedom) increased from 574.9/534 to 584.9/540 for the sharply-broken model, and from 577.6/534 to 588.3/540 for the slowly-bending model. It was thus not significant at greater than the 87% confidence level (in an F-test) to thaw β and γ . With β and γ frozen, f_b , which has typical errors of 0.05 in the log, is seen to increase with increasing photon energy (e.g., errors do not overlap at the 90% confidence level between the M and H bands).

Refitting the PSDs with β , γ and f_b all kept frozen at their average values between the S, M and H bands yields a total (S+M+H) χ^2/dof of 604.2/543 (sharply-broken) and 615.9/543 (slowly-bending). Compared to the model fits with just β and γ frozen, we find that it is significant at $>99.99\%$ confidence in an F-test (for either model) to keep f_b thawed in the fits.

We conclude that the data are not good enough to allow us to distinguish, formally, between a sharp break or a slow rollover in the broken power-law models. However, the data are of high enough quality to conclusively demonstrate a rather unexpected result, one not observed previously in the PSDs of either AGN or XRBs: the break frequency increases with photon energy. This increase in f_b with photon energy holds regardless of whether we use sharply-broken or slowly-bending power law models and whether the power-law slopes in these models are frozen or thawed in the fits. Furthermore, the data are consistent with a broadband PSD shape that is identical for all bands in that the slopes above and below the break are energy-independent; this also has not been previously demonstrated.

Depending on whether the sharply-broken or slowly-bending model is used, and assuming β and γ are energy-independent, we find that from the S to M bands, f_b increases by 0.08 ± 0.08 or 0.05 ± 0.09 in the log; from the M to H bands, f_b increases by 0.13 ± 0.07 or 0.16 ± 0.06 in the log; and from the S to H bands, f_b increases by 0.21 ± 0.08 or 0.21 ± 0.08 in the log. In other words, the change in f_b from the S to H bands is a 2.6σ effect. However, this is a conservative estimate, since the errors in Table 2 are 90%, not 1σ , so the significance of this result is probably larger than 2.6σ . The average photon energy for each

band, weighted for instrument count rate and exposure time, is 0.36, 0.75, and 3.9 keV for the S, M and H bands, respectively. The increase in f_b between the S and H bands is a factor of $\sim 1/5$ times the ratio of the average photon energies.

4.2.2. The Case for a Lorentzian peak in the PSD of Mkn 766

Previous PSD papers have reported that β flattens as photon energy increases while f_b is energy-independent. We fit the S, M and H bands PSDs with the same sharply- or slowly-bending power-law models, but with γ and f_b assumed to be identical for all bands. The best-fit results, calculated by minimizing the sum of χ^2 from the S, M and H bands, are listed in Table 2. The sum of χ^2/dof for the S, M and H bands was 597.5/540 for the sharply-broken model and 599.1/540 for the slowly-bending model. The summed values of χ^2/dof when f_b was allowed to vary in photon energy (γ and β frozen) was 584.9/540 (sharply-broken) or 588.3/540 (slowly-bending). We conclude that a simple broken power-law model where f_b does not vary with energy cannot accurately describe the S, M and H-band PSDs of Mkn 766.

However, there is an alternate model that fulfills the requirements of having f_b energy-independent and providing a good fit to the S, M and H-band PSDs. This is a sharply-broken power-law model with the addition of a Lorentzian component whose strength increases in photon energy:

$$P(f) = \begin{cases} A(f/f_b)^{-\gamma} + P_L + P_{\text{PSn}}, & f \leq f_b \\ A(f/f_b)^{-\beta} + P_L + P_{\text{PSn}}, & f > f_b \end{cases}$$

where

$$P_L = \frac{R^2 f_L Q / \pi}{f_L^2 + Q^2 (f - f_L)^2}$$

f_L is the Lorentzian centroid frequency. Q is the coherence or quality factor. R is the normalization factor of the Lorentzian; for high Q values, R is the fractional rms variability amplitude of the Lorentzian. For values of $Q < 2$, the Lorentzian is very broad and cannot be easily distinguished from band-limited or broadband noise, e.g., the broken power-law component. Lorentzians with higher Q values are called QPOs (e.g., van der Klis 2006).

The addition of the Lorentzian component to the sharply-broken power-law model complicates the model-fitting process. For that reason, in order for the model-fitting results to be reasonable and of some use, we decided to make the following plausible assumptions regarding the parameter values of the Lorentzian component, based mainly on previous results from similar model fits to the XRBs PSDs: First, we are interested in fitting a peak-like component, and so we only consider a Lorentzian with $Q \gtrsim 3$ in order to avoid fitting a component that resembles additional broadband noise. We cannot place tight constraints on Q but have found that values of $\sim 4 - 5$ were the most plausible in terms of providing a good fit to the PSDs. For that reason, all model fits were performed with Q kept fixed at 5. Second, we forced f_L to be the same in all three PSDs (i.e., we assumed that f_L is intrinsically energy-independent) and we further constrained its value to lie in the range $10^{-3.22} - 10^{-3.50}$ Hz; f_L was tested in increments of 0.02 in the log. Finally, R was left as a free parameter, tested in increments of 0.5%. The break

frequency f_b of the broken power-law continuum component was not constrained to be equal for all bands, but was constrained to be $\leq 10^{-3.60}$ Hz. Finally, we left β as a free parameter but kept γ fixed at -1.46 for simplicity.

Table 3 lists the best-fit results obtained from finding the minimum value of χ^2 summed over the S, M and H bands. The data, best fit models, and residuals are plotted in Figure 6. First, we note that both f_b and the power-law slope above the break β are similar for all bands. Second, we find that the best-fit $\log(f_L \text{ (Hz)})$ is -3.34 ± 0.04 ($4.6 \pm 0.4 \times 10^{-4}$ Hz). Finally, we note that R increases with photon energy: it is formally consistent with an upper limit of only 1.5% in the S band, but is $5.5 \pm 0.5\%$ in the H band. This is also demonstrated by Figure 7, which shows derived confidence contours of R versus f_L for each band separately.

Using a slowly-bending model to fit the continuum yielded virtually identical values of χ^2 , R , f_L and identical uncertainties on R and f_L in each band; the best-fit value of f_L was only 0.02 lower in the log compared to using the sharply-broken model.

The temporal frequency resolution of this PSD, despite being the highest for any binned AGN PSD to date, is not high enough to break model degeneracies and simultaneously constrain the curvature of the break and the profile of the Lorentzian component, especially since the Lorentzian is located so close to the break frequency. In addition, the broken power-law model and the model with the Lorentzian component both yield similarly good fits to the PSD, so we cannot exclude one or the other based on the quality of fit alone.

Nonetheless, the PSD is of sufficient quality to detect energy-dependent behavior that has not been observed previously in an AGN. Either f_b increases with photon energy (in which case the broadband PSD shape is likely the same for all energies), or f_b and β are energy-independent and there exists a peak-like component, which we model as a Lorentzian, near 5×10^{-4} Hz whose strength increases with photon energy.

5. CROSS-SPECTRAL PROPERTIES

The cross-spectrum is used to quantify interband correlations as a function of temporal frequency; analogous to the fact that the PSD is the Fourier transform of the ACF, the cross-spectrum is the Fourier transform of the CCF. The cross-spectrum is a complex number; coherence and time lags can be derived from the squared magnitude and argument, respectively. Because these quantities in compact accreting objects tend to be temporal-frequency dependent, they cannot be studied using cross-correlation functions alone. Further details of the cross-spectrum and its relevance to XRB and AGN observations can be found in e.g., Vaughan & Nowak (1997), Nowak et al. (1999a), Papadakis, Nandra & Kazanas (2001) and VFN03.

5.1. The Coherence Function

The coherence function $\gamma^2(f)$ between two time series measures the fraction of mean-squared variability of one series that can be attributed to other, as a function of temporal frequency. If the two time series are related by a simple, linear transfer function, then they will have unity coherence. The coherence is defined as the magnitude

squared of the cross spectrum normalized by the product of each light curve's PSD. Here, we use the discrete versions of the cross-spectrum and coherence functions, given in e.g., §5.2.2 of VF03.

We correct the coherence function for the influence of Poisson noise by following Eq. 8 of Vaughan & Nowak (1997). We assume that the condition of high coherence and high powers required to use this formulation are valid. Specifically, the intrinsic variability power must be at least a factor of a few times $\sqrt{m} \times P_{\text{Psn}}$, where m is the coherence binning factor (quantified below); this condition is thus valid for temporal frequencies up to roughly $1 - 2 \times 10^{-3}$ Hz.

Coherence between the S–M, S–H and M–H band pairs was measured separately for each of the eight light curves, then combined, sorted in temporal frequency, and binned in groups of $m=30$ to form the final coherence function estimate. As shown in Figure 8, the coherence is near unity ($\gtrsim 0.8 - 0.9$) over the lowest temporal frequencies sampled for the S–M and M–H pairs. For S–H, the coherence is a bit lower, $\sim 0.6 - 0.8$, at these temporal frequencies. At the highest temporal frequencies sampled, the coherence significantly drops sharply towards zero in all cases.

This cutoff at high temporal frequencies can be intrinsic, but could also be due to Poisson noise. Monte Carlo simulations were used as a check on the accuracy of the coherence estimates and to determine if significant deviations from unity could be attributed to the effect of Poisson noise. For the 2005 long-look, two light curves of duration several Msec were simulated using the same random number seed and assuming identical PSD shapes (the average of the best-fitting singly-broken PSD model for each band pair) to produce two light curves with intrinsic unity coherence. The simulated light curves were rebinned and resampled to match the observed light curves (e.g., broken into seven smaller light curves matching the sampling of the observed ones), and rescaled to match the mean observed count rates in the softer and harder bands. Poisson noise was then added to the data according to the Poisson distribution, i.e., data were randomly deviated using a Gaussian convolved with the square root of the observed mean error squared divided by the sampling time. Simulated light curves for the 2001 data were produced in the same way. One hundred sets of simulated data were produced. For each set, the coherence and its uncertainty was calculated as for the real data (e.g., combining the eight simulated light curves). At most temporal frequencies below $\sim 10^{-3}$ Hz, the simulated coherence was reasonably close to unity, and the uncertainty in the coherence was in reasonable agreement with the scatter, indicating that the coherence estimation was reasonably accurate. The 90% and 95% lower limits to the coherence were determined. Any measurement of the observed coherence function lying below these lines thus indicates a drop in coherence that is intrinsic to the source, and not an artifact of the Poisson noise, at 90% or 95% confidence. For most temporal frequencies below $\sim 10^{-3.5}$ Hz, the artificial drop in coherence is small.

The energy-dependence of the high-frequency PSD slope could also contribute to a reduction in measured coherence. The Monte Carlo simulations were repeated, assuming the best-fit sharply-broken power-law model shapes.

The effects of Poisson noise were again added. The simulated coherence was typically only $\sim 1\%$, $3 - 4\%$ and $1 - 3\%$ lower for the S–M, S–H and M–H bands, respectively, compared to simulations assuming identical PSD shapes. The effect of having differing PSD shapes is thus small. The 90% and 95% lower limits to the coherence were determined and are plotted in Figure 8. The observed deviations from unity are generally larger than the artificial drop due to Poisson noise. The decrease in intrinsic coherence as the energy separation of the bands increases and as temporal frequency increases towards $\sim 10^{-3}$ Hz is also likely intrinsic.

Having quantified the decrease in coherence e.g., due to Poisson Noise at each temporal frequency, we added the mean value of the drop in coherence from the Monte Carlo simulations to the observed coherence to obtain an estimate of the 'intrinsic' coherence, plotted in the bottom panel of Figure 8. We fit the 'intrinsic' coherence functions with exponential decay functions of the form $\gamma^2(f) = C \exp(-(f/f_c)^2)$, where f_c is the temporal frequency cutoff in Hz and C is a constant, ignoring points above 1.2×10^{-3} Hz, and using least-squares fitting, assuming equal weighting to all points. We find that $\log(f_c)$ for the S–M, S–H and M–H coherence functions are -2.82 ± 0.03 , -2.80 ± 0.03 and -2.81 ± 0.03 , respectively.

5.2. Temporal Frequency-Dependent Time Lags

Cross-correlation functions (CCFs) for XRBs and AGN generally show a peak near zero lag but are often asymmetrically skewed towards hard lags (e.g., M^cHardy et al. 2004), suggesting there is a soft-to-hard time lag of some sort, but it is not a simple delay. We measured the CCFs for the 2005 data using e.g., the Interpolated Correlation Function (White & Peterson 1994). Because large gaps such as those between revolutions complicate analysis, we calculated CCFs for each individual revolution separately. As expected, all peak lags are consistent with zero and CCFs exhibit a slight soft-to-hard asymmetric skew. The logical direction is to explore temporal frequency-dependent time lags via the cross-spectrum.

Obtaining sensible measurements of time lags via the cross-spectrum is difficult for observations of AGN, however; it requires the combination of a large quantity of uninterrupted data with a high sampling time resolution and a high variability-to-Poisson noise ratio. VF03 did not present lags for the 2001 data; we also attempted to derive time lags from the 2001 pn data and did not detect any obvious time lag trends, likely due to the combination of intrinsically small lag values (see below), high scatter, and low temporal frequency resolution.

We used Eqs. 28 and 29 in §5.3.1 of VF03 to calculate the phase lags $\phi(f)$; time lags were then obtained as $\tau(f) = \phi(f)/2\pi f$. Time lags were calculated for each of the eight light curves separately, then combined, sorted in frequency, and binned in groups of 50. Errors on phase lags were calculated using Eq. 16 of Nowak et al. (1999a); in this formulation we used the coherence function appropriate for each binned point. Sensible lags (e.g., lags all have the same sign and show a trend) were obtained for the 4 lowest temporal frequency bins, spanning $4.4 \times 10^{-5} - 3.3 \times 10^{-4}$ Hz. The results are shown in Figure 9. Errors are large, primarily because coherence in this

temporal frequency range is not always exactly unity. Using Eq. 16 in Nowak et al. (1999a), we estimated the effective sensitivity limit on time lag detections due to Poisson noise, using the PSD shape and normalization from best-fit M-band singly-broken PSD model shape in §4. Limits are shown as dotted lines in Figure 9.

Monte Carlo simulations, based on the simulated light curves used for the coherence functions, were performed to verify that the time lags were not an artifact of Poisson noise nor of the differing PSD slopes between two bands. For all simulations, time lags were <24 s for the two lowest temporal frequency bins and <15 s for the next two bins. We can reasonably conclude that the observed time lags are not an artifact of Poisson noise or PSD shape differences, and are henceforth assumed intrinsic to the source.

The time lag spectrum displays the general qualities seen in many previous time lag spectra: a general increase towards lower temporal frequencies and as the energy separation of the bands increases. Assuming that the time lags are proportional to $\tau(f) = Cf^{-1}$ for simplicity allows us to calculate fractional time lags, i.e., the lags' fraction of the temporal frequency. We find that $C = 0.002, 0.009$, and 0.007 for S–M, S–H and M–H, respectively. These values of C are roughly correlated with values of $\log(E_2/E_1) = 0.32, 1.03$ and 0.72 , respectively, where E_1 and E_2 are the relatively softer and harder average photon energies in each band (§4.2.1). Similar correlations have been reported previously in XRBs and in the NL Sy1 Ark 564 (Arévalo et al. 2006a). The physical implications of these time lags and comparisons to other objects will be discussed further in §6.

6. DISCUSSION

An *XMM-Newton* observation of Mkn 766 spanning six revolutions in 2005 caught the source in a relatively low flux state; with the average 0.2–12 keV flux about half of the flux during the 107 ksec *XMM-Newton* observation in 2001. Reduction of the 2005 observation yielded seven long, virtually uninterrupted light curves of this highly-variable source totaling 442 ksec of good exposure time.

We find no evidence for the underlying variability process to have changed from 2001 to 2005, despite a factor of 2 difference in average flux. Specifically, the PSD shapes and coherence functions between 2001 and 2005 are consistent and both observations appear to have consistent linear rms-flux relations and constant $\langle F_{\text{var}} \rangle$ values. The Mkn 766 light curves are thus stationary over a four year duration as far as the second-order moments are concerned.

Combining the 2005 and 2001 observations, we have constructed a binned PSD with the highest temporal frequency resolution in log space for an AGN PSD to date. We find energy-dependent behavior not reported previously in AGN PSDs, as discussed in §6.1. In addition, time lags have been detected in Mkn 766 for the first time; §6.2 discusses the cross-spectral results and compares them to those of other compact accreting objects. Finally, the results are discussed in the context of phenomenological variability models in §6.3.

6.1. Summary of PSD Results

The high temporal frequency resolution of the PSDs allows us to place tight constraints on localized features

(a PSD break or the presence of a peak-like feature, i.e., a QPO) in any model we fit. Our initial approaches to model the PSD centered on broken power models. Model fits cannot formally distinguish between a sharp break or a slow rollover, despite the high frequency resolution; both models fit the data well. In general, there are no obvious trends in the power-law slope above or below the break, suggesting the existence of a “universal” PSD shape at all bands whose break scales with photon energy. In that case, fit parameters may depend on the temporal frequency range being studied. Our main result is that f_b increases with photon energy. Neither the increase in f_b nor an energy-independent PSD shape has been conclusively demonstrated previously in AGN.

6.1.1. The increase in f_b with photon energy

Our estimate for the T-band break frequency is $\log(f_b) = -3.36 \pm 0.04$ (sharply-broken model, all parameters free). This value is consistent with that of VF03, but the uncertainty is much lower compared to VF03 or even to VFN03 for the three *XMM-Newton* revolutions of data for MCG-6-30-15. For the first time in an AGN PSD, the break frequency is seen to increase with energy, a result that is robust to the specific broken power-law model shape used. The break frequency tends to increase by $\sim 0.2 - 0.4$ in the log between the S and H bands (a factor of ~ 10 in average photon energy).

Most previous Seyfert PSDs simply did not have sufficient temporal frequency resolution to detect significant changes in f_b with photon energy such as those seen here. It is plausible that for a limited dynamic range PSD with low frequency resolution, the effect of having f_b intrinsically increasing with photon energy could lead instead to apparent measurements of the power-law slope above the break, β , flattening with energy. Indeed, when we fit the Mkn 766 PSD with γ and f_b frozen, β flattens with energy, suggesting that previously observed trends of β with photon energy may instead be due to an intrinsic energy dependence of f_b . Alternatively, it could be the case that this phenomenon might exist only in Mkn 766; high-quality, high-resolution PSDs are needed for a sample of Seyferts to determine whether this is the case.

The fact that the observed increase in f_b with energy is small suggests that PSD measurement spanning a range of photon energies wider than those used here would be needed to further separate f_b in energy. In the case of XRBs, it is possible that this phenomenon may not have been reported due to insufficient spread in the hard X-ray photon energies studied.

6.1.2. The possible presence of a Lorentzian component

The alternate to modeling the PSD with f_b as a free parameter is to assume that f_b is energy-independent. Achieving a good fit requires the presence of a peak-like component, which we model as a Lorentzian with $Q = 5$, that is centered at $4.6 \pm 0.4 \times 10^{-4}$ Hz and whose rms variability R increases from $< 1.5\%$ in the soft band to $5.5 \pm 0.5\%$ in the hard band. Such a detection, though model-dependent, is also a new result for AGN.

Following the definition of van der Klis (2006), the Lorentzian component can be identified as a QPO. Most previous reports of deterministic behavior or claims of

QPOs in AGN have been refuted, have failed the test of repeated observations, or did not use the appropriate statistical significance tests (see Vaughan & Uttley 2005 and Vaughan 2005). We are basing our claim on modeling of a PSD that is properly binned, has well-defined errors, has very high temporal frequency resolution, and is derived from a large quantity of high-quality data. We sample almost 300 cycles of this feature throughout the duration.

We reiterate that our claim of the presence of a QPO in the PSD is highly model-dependent, since a simple broken power-law model can fit the data well. The requirement for the QPO arises only when f_b is assumed to be energy-independent. Both models adequately describe the energy dependence of the PSD well, though Occam's Razor may have one prefer the simple, broken-power law model, since it consists of only the broadband PSD component and does not make any *a priori* assumption about the behavior of f_b with energy.

Assuming that the QPO at 4.6×10^{-4} Hz is real, there are intriguing similarities to those observed in XRBs. QPOs whose rms variability R increases with photon energy have been observed in XRBs. For example, the 450 Hz QPO in GRO J1655–40 and the 40 Hz QPO in GRS 1915+105 are detected only above 13 keV by Strohmayer et al. (2001a) and (2001b), respectively. In Mkn 766, the value of R is highly model-dependent, but also increases with photon energy and displays roughly similar values, from $< 1.5\%$ at ~ 0.4 keV to 5.5% at ~ 4 keV. It is not unreasonable to compare the (relatively softer) energy bands in Mkn 766 with the (harder) energy bands in XRBs, since softer bands in XRBs may be dominated by thermal disk emission.

Photon indices in the low/hard, high/soft and very high state in XRBs tend to be $\sim 1.5 - 2.0$, $\gtrsim 2 - 3$, and $\sim 2.4 - 2.9$, respectively (e.g., McClintock & Remillard 2006; Homan et al. 2005). The photon index of the power-law continuum in Mkn 766 is $\sim 2.3 - 2.4$ (e.g., Turner et al. 2006, Miller et al. 2006). A direct comparison between Mkn 766 and XRBs in the very high state therefore might not be rejected on those grounds. QPOs, however, tend to appear only in XRB states when the thermal disk emission does not dominate the energy spectrum (van der Klis 2006, McClintock & Remillard 2006). The existence of a QPO in Mkn 766 would therefore argue against Mkn 766 being an analog of the (thermal-dominated) high/soft state in XRBs.

One may ask whether the possible QPO in Mkn 766 is the analog of low-frequency (LF) or high-frequency (HF) QPOs. Type A and B LF QPOs usually appear at 4–9 Hz. Assuming that QPO frequencies scale linearly with black hole mass, and assuming $10 M_\odot$ for the mass of stellar-mass black holes, the mass of the black hole in Mkn 766 is thus estimated to be $1 - 2 \times 10^5 M_\odot$. This is somewhat low compared to estimates of Mkn 766's black hole mass: Botte et al. (2005) measure a stellar velocity dispersion σ_* of 81 ± 17 km s $^{-1}$ in Mkn 766. Using the relation between σ_* and M_{BH} as parameterized by Tremaine et al. (2002), this suggests $M_{\text{BH}} = 3.6_{-1.9}^{+3.5} \times 10^6 M_\odot$. Estimates using the width of the H β line and the Kaspi et al. (2000) relation lie in the range $0.8 - 10.0 \times 10^6 M_\odot$ (Wandel 2002; Bian & Zhao, 2003a, 2003b, 2004; Botte et al. 2005). On the other hand, the fact that XRB QPOs tend to appear

only in states when the thermal disk emission does not dominate the energy spectrum suggests that QPOs are associated with the corona instead of the disk (Reig et al. 2006; van der Klis 2006, McClintock & Remillard 2006). QPO frequencies may thus scale with some other property besides or in addition to black hole mass. Type C LF QPOs tend to have R values which may be too high to compare to Mkn 766.

HF QPOs usually are seen near 100–300 Hz, and usually with $R \sim 1 - 3\%$. They are often found in pairs, at frequencies of 2 and 3 times an unseen “fundamental” frequency f_0 . The Mkn 766 PSD does not have the resolution to determine if the QPO corresponds to the $2f_0$ or the $3f_0$ peak being dominant, or if it is a blend of the two. Based on observations of three black hole XRBs, McClintock & Remillard (2006) have suggested that f_0 scales linearly with black hole mass M_{BH} as $931 \text{ Hz } (M_{\text{BH}}/M_\odot)^{-1}$, assuming similar values of the spin parameter; this linear scaling suggests that HF QPOs in black holes may represent disk oscillations described by general relativity (see Abramowicz & Kluzniak 2001). Extrapolating this relation to Mkn 766 and assuming $f_0 = 1.8 - 2.4 \times 10^{-4}$ Hz, this implies a black hole mass of $3.9 - 5.2 \times 10^6 M_\odot$, consistent with the optically-estimated black hole masses. On the other hand, HF QPOs are not always found very close to the break in the broadband component, as is the case here.

In the end, the community needs very high-quality data on a reasonably sized sample of AGN to be able to confirm or refute the presence of QPOs in AGN in order to shore up the comparisons between AGN and XRBs. The Mkn 766 observations are an important step towards this goal, demonstrating that high-quality data in the form of a collection of long, uninterrupted exposures can successfully yield an enormous payoff for AGN variability investigations.

6.2. Summary of cross-spectral results and comparison to other objects

The coherence is generally flat at the lowest temporal frequencies probed, with values typically $\sim 0.8 - 0.9$ for S–M and M–H and $\sim 0.6 - 0.8$ for S–H. The coherence drops towards zero near $\sim 10^{-3}$ Hz; Monte Carlo simulations prove that these deviations from unity are intrinsic to the source and not the result of Poisson noise or energy-dependent PSD shapes. The decrease in coherence as energy separation increases has been reported previously for Mkn 766 by VF03; we in fact see values of the coherence similar to VF03. This similarity again supports the conclusion of §3, that there is no evidence for the underlying variability process to have changed significantly between 2001 and 2005 despite the overall lower average flux in 2005.

In other black hole systems, the coherence at temporal frequencies below the break is generally between 0.8 and 1.0, though coherence between bands similar to the S and H bands used here can be as low as $\sim 0.6 - 0.7$ (e.g., VFN03 & M^cHardy et al. 2004); Mkn 766's coherence functions thus agree with those in other compact objects. As explained in Vaughan & Nowak (1997), coherence between two energy bands can be lost if the transfer function relating the light curves is non-linear, or if there are multiple

uncorrelated flaring regions. The fact that coherence in Mkn 766 and several other compact objects is not exactly unity may support some degree of non-linearity present in the transfer functions relating relatively softer and harder bands, and which increases for larger energy separations.

The coherence function between the S and H bands drops to $\sim 1/e$ around 1×10^{-3} Hz in both MCG-6-30-15 (VFN03) and Mkn 766, while the drop in NGC 4051's S-H coherence occurs at roughly $\sim 4 \times 10^{-3}$ Hz (M^cHardy et al. 2004). MCG-6-30-15's black hole mass is roughly $3 \times 10^6 M_{\odot}$ (M^cHardy et al. 2005), similar to that for Mkn 766, while that for NGC 4051 is $1.9 \pm 0.8 \times 10^6 M_{\odot}$ (Peterson et al. 2004). A larger sample of coherence functions of Seyferts spanning a larger black hole mass range is needed to verify if coherence time scales scale with black hole mass, just as PSD break time scales do.

As explained by e.g., Nowak & Vaughan (1996) and Nowak et al. (1999a), the sharp drop in coherence at temporal frequencies above the PSD break could indicate that the corona is dynamic on such short time scales. Such short time scales could be associated with formation time scales or changes in temperature and/or the physical structure of the corona. The relatively high levels of coherence at low temporal frequencies could indicate that the corona is effectively static on long time scales.

We measure temporal-frequency dependent phase lags in Mkn 766 for the first time; lags increase towards lower temp frequency and as energy separation of bands increases, as seen in other black hole systems. Fractional time lags are about 0.01–0.02 the Fourier time scale. These values are consistent with most values measured so far for other AGN and many XRBs (see e.g., Figure 8 of Arévalo et al. 2006a), with fractional time lags usually measured to be $\lesssim 0.2$, though Ark 564's time lag spectrum (Arévalo et al. 2006a) seems to be an exception among AGN.

Assuming a PSD break frequency of $10^{-3.4}$ Hz, the Mkn 766 lag spectrum is probing temporal frequencies 0.14 – 1.00 times the break frequency. We can compare Mkn 766's fractional lags to those measured for Cyg X-1 within \pm a decade of temporal frequency of the PSD breaks. In the low/hard and high/soft state of Cyg X-1, fractional time lags tend towards 0.03–0.1 (e.g., Nowak et al. 1999a), while in the intermediate state, fractional time lags are higher, $\sim 0.1 – 0.2$ (e.g., Pottschmidt et al. 2000). On the basis of these fractional lag values, Mkn 766 is likely not a supermassive analog of Cyg X-1 in the intermediate-state, though we cannot determine on the basis of lags alone if analogy with the low/hard or high/soft state is appropriate. Furthermore, the time lag spectrum is not of high enough quality to distinguish between an intrinsic lag spectrum which is step-like, as in the intermediate state of Cyg X-1, or adheres to a form more resembling a power-law.

6.3. Phenomenological Variability Models

Many models have been invoked to explain the red noise variability properties of Seyferts and XRBs, including shot-noise models (e.g., Merloni & Fabian 2001), rotating hot-spots on the surface of the accretion disk (Bao & Abramowicz 1996), self-organized criticality ("pulse avalanche" models; Mineshige, Ouchi & Nishimori 1994), magnetohydrodynamical instabilities in the disk (Hawley

& Krolik 2001), and inwardly-propagating fluctuations in the local accretion rate (Lyubarskii 1997). As noted by Uttley, M^cHardy & Vaughan (2005), shot-noise models have difficulty reproducing the linear rms-flux relation, and, as noted by Vaughan & Nowak (1997), they lead to low observed coherence values unless each separate emitting region independently has the same linear transfer function between energy bands.

Thermal Comptonization of soft seed photons by a hot corona is a likely explanation for the X-ray emission. It is supported by X-ray energy spectra, and the soft-to-hard time lags could be attributed to the time scale for seed photons to diffuse through the corona and undergo multiple up-scatterings. However, the simplest Comptonization models do not predict time lags that depend on temporal frequency, as observed.

A model in which inwardly-propagating variations in the local mass accretion rate \dot{m} are responsible for the observed X-ray variability seems to be able to explain many of the observational results in Seyferts and XRBs (Lyubarskii 1997, Churazov, Gilfanov & Revnivtsev 2001), Kotov et al. 2001, Arévalo & Uttley 2006; see also VFN03 and M^cHardy et al. 2004). In this model, variations at a given radius are associated with the local viscous time scale, so relatively smaller radii are associated with relatively more rapid variations. Perturbations in \dot{m} propagate inward, until they reach, and modify the emission of, the central X-ray emitting region. The resulting PSD has a $1/f$ form across a broad range of temporal frequencies, the net sum of variations from a wide range of radii. However, if the X-ray emitting region is extended, it essentially acts like a low-pass filter on these $1/f$ variations: with relatively higher-frequency variations imprinted on the light curve originating only from the smallest radii, this produces a cutoff in the high-frequency PSD, as is commonly observed. Kotov et al. (2001) suggested that the spectrum can be a function of radius, with relatively harder emission emanating from smaller radii, and therefore associated with more rapid variability. This class of models thus predicts several additional properties which are observed in Seyferts and XRBs, namely the presence of the linear rms-flux relation, and the dependence of coherence and time lags on temporal frequency and on the energy separation of the bands.

Arévalo & Uttley (2006) show that if relatively harder X-ray bands are associated with emissivity profiles that are more centrally concentrated, and if the PSD break is at least partly due to filtering produced by having an extended X-ray emission region, then the harder bands will retain more variability power at the highest temporal frequencies, leading to break frequencies in the broadband PSD which increase with increasing photon energy. We note that the PSDs of Mkn 766 as shown in Figure 5b, bear a striking qualitative resemblance to the simulated PSDs in Figure 2 of Arévalo & Uttley (2006). The degree of curvature in the Mkn 766 PSDs is uncertain, and rollover frequencies are relatively close together, so it is not straightforward to relate break frequencies to emissivity index or profile. However, we note that the 'soft' and 'hard' PSDs in Figure 2 of Arévalo & Uttley (2006), simulated assuming emissivity indices which differ by 2, yield break frequencies which are separated by about a decade.

In Mkn 766, the S- and H-band break frequencies are not as separated, suggesting that, in the context of this model, the emissivity indices for the S- and H- bands differ by less than 2. The relatively small fractional time lags observed in Mkn 766 (0.01–0.02 for the S–H bands) are consistent with a difference in emissivity indices of ~ 0.5 to a few.

7. CONCLUSIONS

We have analyzed the energy-dependent variability properties of the Narrow Line Seyfert 1 Mkn 766 using light curves obtained from two *XMM-Newton* observations. An observation spanning six revolutions in 2005 yielded seven uninterrupted EPIC light curves totaling 442 ksec of good exposure time; an observation in 2001 yielded an eighth uninterrupted light curve with an exposure of 107 ksec. A linear rms-flux relation, or equivalently, constant $\langle F_{\text{var}} \rangle$, was reported for the 2001 observation by Vaughan et al. (2003a). These relations are confirmed for the 2005 observation, and shown to be consistent with the corresponding relations from the 2001 observation. Comparing the 2001 and 2005 PSDs shows the PSDs to be consistent within the expected scatter. Variability properties between the 2005 and 2001 observations are thus consistent with each other, despite a 0.2–12 keV flux in 2005 which is about half that of the 2001 observation. We combined the 2001 and 2005 data sets in order to probe power- and cross-spectral properties with temporal frequency resolution that is unprecedented for an AGN.

We have explored two parameterizations of the energy-dependent PSD. Both fit the data equally well, but in either case, they signify behavior never seen previously in an AGN PSD. Fitting simple broken power-laws, we find PSD breaks at nearly the same temporal frequencies as VF03, but the break frequencies f_b are seen to increase with photon energy, typically by ~ 0.2 – 0.3 in the log between ~ 0.4 keV and ~ 4 keV emission. There is no obvious trend in PSD power-law slope, and the data are consistent with a universal PSD shape whose break frequency increases with photon energy. Previous Seyfert PSDs lacked the temporal frequency resolution to cleanly detect the energy de-

pendence in f_b . Keeping f_b fixed with energy does not provide a good description of the energy-dependent PSD. However, we can achieve a good fit using a sharply-broken power-law, where the break frequency and power-law slope above the break are roughly energy-independent, but we must include a narrow peak component, i.e., a QPO, at $4.6 \pm 0.4 \times 10^{-4}$ Hz. Interestingly, the rms variability amplitude of this QPO increases with photon energy in a manner similar to QPOs seen in the PSDs of black hole XRBs.

Cross-spectral properties are qualitatively consistent with those measured for black hole systems previously. The coherence is generally flat at the lowest temporal frequencies probed, with values typically ~ 0.6 – 0.9 . The coherence drops towards zero at temporal frequencies higher than roughly $10^{-2.8}$ Hz; Monte Carlo simulations indicate that the drop is intrinsic to the source and not an artifact of Poisson noise or differing PSD shapes.

Temporal frequency-dependent time lags are measured from the cross-spectrum for the first time in Mkn 766. As is the case with time lags in other objects, lags increase as temporal frequency increase and as energy separation of the light curves increases. Fractional time lags are typically $\lesssim 0.01$, consistent with many other Seyferts as well as with the high/soft and low/hard states of Cyg X-1.

The results were discussed in the context of several variability models, including models incorporating inwardly-propagating fluctuations in the local mass accretion rate, e.g., Lyubarskii (1997). Notably, the observed increase in the PSD break frequency with photon energy is qualitatively consistent with the prediction put forth by e.g., Arévalo & Uttley (2006), who model variations in a disk with relatively harder X-ray emission being more centrally concentrated.

We thank the referee for providing useful comments. This work has made use of observations obtained with *XMM-Newton*, an ESA science mission with instruments and contributions directly funded by ESA member states and the US (NASA).

REFERENCES

Abramowicz, M.A. & Kluzniak, W. 2001, A&A, 374, L19
 Arévalo, P. et al. 2006a, MNRAS, 401, 372
 Arévalo, P. et al. 2006b, in prep. (Paper III)
 Arévalo, P. & Uttley, P. 2006, MNRAS, 367, 801
 Axelsson, M., Borgonovo, L. & Larsson, S. 2005, A&A, 438, 999
 Bao, G. & Abramowicz, M. 1996, ApJ, 465, 646
 Bevington, P. R. 1969, *Data Reduction and Error Analysis for the Physical Sciences* (New York: McGraw-Hill)
 Bian, W. & Zhao, Y. 2003a, MNRAS, 343, 164
 Bian, W. & Zhao, Y. 2003b, ChJAA, 3, 119
 Bian, W. & Zhao, Y. 2004, MNRAS, 352, 823
 Botte, V., Ciroi, S., di Mille, F., Rafanelli, P. & Romano, A. 2005, MNRAS, 356, 789
 Churazov, E., Gilfanov, M. & Revnivtsev, M. 2001, A&A, 321, 759
 Edelson, R. et al. 2002, ApJ, 568, 610
 Gilfanov, M., Churazov, E. & Revnivtsev, M. 2000, MNRAS, 316, 923
 Hawley, J.F. & Krolik, J.H. 2001, ApJ, 548, 348
 Homan, J. et al. 2005, ApJ, 623, 383
 Kaspi, S., Smith, P.S., Netzer, H., Maoz, D., Jannuzzi, B.T., Giveon, U., 2000, ApJ, 533, 631
 Kotov, O., Churazov, E. & Gilfanov, M. 2001, MNRAS, 327, 799
 Leighly, K.M. 2004, Prog. Theor. Phys. Suppl., 155, 223
 Lin, D., Smith, I.A., Böttcher, M., Liang, E.P. 2000, ApJ, 531, 963
 Lyubarskii, Y.E. 1997, MNRAS, 292, 679
 Markowitz, A. et al. 2003, ApJ, 593, 96
 Markowitz, A. 2005, ApJ, 635, 180
 McClintock, J.E. & Remillard, R.A., 2006, in *Compact Stellar X-Ray Sources*, eds. W.H.G. Lewin & M. van der Klis (Cambridge: Cambridge University Press), in press (astro-ph/0306213)
 McHardy, I.M., Papadakis, I., Uttley, P., Page, M.J. & Mason, K.O. 2004, MNRAS, 348, 783
 McHardy, I.M., Gunn, K.F., Uttley, P. & Goad, M.R. 2005, MNRAS, 359, 1469
 Merloni, A. & Fabian, A.C. 2001, MNRAS, 328, 958
 Miller, L. et al. 2006, A&A, submitted
 Mineshige, S., Ouchi, N.B. & Nishimori, H. 1994, PASJ, 46, 97
 Miyamoto, S., Kimura, K., Kitamoto, S., Dotani, T. & Ebisawa, K. 1991, ApJ, 383, 784
 Miyamoto, S. & Kitamoto, S. 1989, Nature, 342, 773
 Nandra, K. & Papadakis, I. 2001, ApJ, 554, 710
 Nowak, M. 2000, MNRAS, 318, 361
 Nowak, M. & Vaughan, B. 1996, MNRAS, 280, 227
 Nowak, M., Vaughan, B., Wilms, J., Dove, J., & Begelman, M. 1999a, ApJ, 510, 874
 Nowak, M., Wilms, J., & Dove, J. 1999b, ApJ, 517, 355
 Oppenheim, A. & Schafer, R. 1975, “Digital Signal Processing,” (Prentice-Hall Publishing)
 Papadakis, I. et al. 2006, in prep. (Paper II)
 Papadakis, I., Kazanas, D. & Akylas, A. 2005, ApJ, 631, 727
 Papadakis, I. & Lawrence, A. 1993, MNRAS, 261, 612
 Papadakis, I. & Lawrence, A. 1995, MNRAS, 272, 161

Papadakis, I., Nandra, K. & Kazanas, D. 2001, ApJ, 554, L133
 Peterson, B.M. et al. 2004, ApJ, 613, 682
 Pottschmidt, K. et al. 2000, A&A, 357, L17
 Pounds, K.A., Reeves, J.N., Page, K.L., Wynn, G.A. & O'Brien, P.T. 2003, MNRAS, 342, 1147
 Priestley, M. 1981, "Spectral Analysis and Time Series," (London: Academic Press Ltd.)
 Reig, P., Papadakis, I.E., Shrader, C.R. & Kazanas, D. 2006, ApJ, 644, 424
 Shapiro, S., Lightman, A. & Eardley, D. 1976, ApJ, 204, 187
 Strohmayer, T.E. 2001a, ApJ, 552, L49
 Strohmayer, T.E. 2001b, ApJ, 554, L169
 Strüder, L. et al. 2001, A&A, 365, L18
 Sunyaev, R. & Titarchuk, L. 1980, A&A, 86, 121
 Tremaine, S. et al. 2002, ApJ, 574, 740
 Turner, M.J.L. et al. 2001, A&A, 365, L27
 Turner, T.J. et al. 2006, in prep.
 Uttley, P. & M^cHardy, I.M. 2001, MNRAS, 323, L26
 Uttley, P., M^cHardy, I.M. & Papadakis, I.E. 2002, MNRAS, 332, 231
 Uttley, P., M^cHardy, I.M. & Vaughan, S. 2005, MNRAS 359, 345
 van der Klis, M. 1997, in Statistical Challenges in Astronomy II, ed. G.J. Babu & E.D. Feigelson (New York: Springer), 321
 van der Klis, M. 2006, in Compact Stellar X-Ray Sources, eds. W.H.G. Lewin & M. van der Klis (Cambridge: Cambridge University Press), in press (astro-ph/0410551)
 Vaughan, B. & Nowak, M. 1997, ApJ, 474, L43
 Vaughan, S. 2005, A&A, 431, 391
 Vaughan, S., Edelson, R., Warwick, R. & Uttley, P. 2003a, MNRAS, 345, 1271
 Vaughan, S. & Fabian, A. 2003, MNRAS, 341, 496
 Vaughan, S., Fabian, A. & Nandra, K. 2003b, MNRAS, 339, 1237 (VFN03)
 Vaughan, S. & Uttley, P. 2005, MNRAS, 362, 235
 Wandel, A. 2002, ApJ, 565, 762
 White, R. & Peterson, B.M. 1994, PASP, 106, 978
 Zdziarski, A., Lubinski, P., Gilfanov, M. & Revnivtsev, M. 2003, MNRAS, 342, 355

APPENDIX

PSD CONSISTENCY

We tested for strong non-stationarity in the form of a change in the shape of the underlying PSD, between the 2001 and 2005 PSDs and between revolutions in the 2005 long-look. For two PSDs observing the same stationary process at two different times, the only difference in PSD values at a given temporal frequency should be consistent with the expected scatter. The scatter in the measured PSD about the intrinsic, underlying PSD follows a χ^2 distribution with two degrees of freedom (e.g., Priestley 1981); Papadakis & Lawrence (1995) thus outlined a method to test for non-stationarity, defining a statistic S to quantify differences between two PSDs. For a stationary process, S will be distributed with a mean of 0 and a variance equal to 1 (see also VFN03).

We considered PSDs for each revolution from 999 to 1003A using the summed pn + MOS1+MOS2 T, S, M and H-band light curves as well as for the summed pn + MOS2 light curve from 2001. Light curves were binned to 60 seconds and truncated to a common duration of 52.6 ksec; PSDs were generated by binning periodogram points by a factor of 25.

The S statistic was calculated by summing over temporal frequencies $<10^{-2.6}$ Hz to exclude PSD points that were dominated by power due to Poisson noise. For all PSD pairs and bands, $|S|$ was found to 0.54 or less. Extending the duration to 74.0 ksec to compare revolutions 265 and 999–1002 and extending the duration to 92.2 ksec to compare revolutions 265 and 1000–2 also yielded similarly small values of $|S|$ ($\lesssim 0.5$) for all bands. To summarize, all values of $|S|$ were less than 1 for all light curve pairs and bands; we therefore have found no evidence at 1σ confidence or greater for strong non-stationarity in the PSDs of Mkn 766 at any band from one revolution to the next in the 2005 long-look, or between 2001 and 2005.

TABLE 1
 UNBROKEN POWER-LAW MODEL FITS TO THE PSD

Band	χ^2/dof	β	A
T	299.3/180	2.34 ± 0.06	0.99 ± 0.03
S	137.4/180	2.14 ± 0.08	0.79 ± 0.04
M	258.3/180	2.22 ± 0.06	1.00 ± 0.03
H	278.4/180	2.14 ± 0.08	1.16 ± 0.03

Note. — A is the PSD amplitude in units of Hz^{-1} at $f_0 = 10^{-3.50}$ Hz.

TABLE 2
SHARPLY- AND SLOWLY BROKEN POWER-LAW MODEL FITS TO THE PSDS

Band	χ^2/dof	γ	$\log(f_b(\text{Hz}))$	β	A
Sharply-Broken Power-Law Model Fits					
T	207.5/178	1.48 \pm 0.14	-3.36 \pm 0.04	3.00 \pm 0.12	0.95 \pm 0.03
S	217.9/178	1.56 \pm 0.18	-3.55 \pm 0.09	2.56 $^{+0.16}_{-0.14}$	1.08 \pm 0.04
M	173.0/178	1.54 \pm 0.14	-3.34 \pm 0.05	3.10 \pm 0.18	0.91 \pm 0.03
H	178.0/178	1.28 \pm 0.12	-3.29 \pm 0.04	3.02 \pm 0.16	1.01 \pm 0.03
T	208.6/180	1.46 (fixed)	-3.39 \pm 0.05	2.89 (fixed)	0.99 \pm 0.03
S	222.6/180	1.46 (fixed)	-3.48 \pm 0.06	2.89 (fixed)	1.00 \pm 0.04
M	175.1/180	1.46 (fixed)	-3.40 \pm 0.05	2.89 (fixed)	1.03 \pm 0.03
H	187.2/180	1.46 (fixed)	-3.27 \pm 0.05	2.89 (fixed)	0.92 \pm 0.03
T	207.6/180	1.46 (fixed)	-3.36 (fixed)	3.00 \pm 0.14	0.94 \pm 0.03
S	231.6/180	1.46 (fixed)	-3.36 (fixed)	2.94 \pm 0.24	0.73 \pm 0.04
M	173.4/180	1.46 (fixed)	-3.36 (fixed)	3.08 $^{+0.22}_{-0.16}$	0.97 \pm 0.03
H	192.5/180	1.46 (fixed)	-3.36 (fixed)	2.76 \pm 0.14	1.10 \pm 0.03
Slowly-Broken Power-Law Model Fits					
T	210.8/178	1.26 \pm 0.12	-3.34 \pm 0.05	3.34 \pm 0.12	-3.10 \pm 0.03
S	218.3/178	1.04 \pm 0.24	-3.77 \pm 0.09	2.68 \pm 0.12	-2.16 \pm 0.04
M	172.9/178	1.42 \pm 0.12	-3.23 \pm 0.06	3.72 \pm 0.22	-3.73 \pm 0.03
H	186.4/178	1.16 \pm 0.10	-3.20 \pm 0.04	3.58 \pm 0.20	-2.70 \pm 0.03
T	210.9/180	1.21 (fixed)	-3.36 \pm 0.05	3.33 (fixed)	-2.91 \pm 0.04
S	225.5/180	1.21 (fixed)	-3.44 \pm 0.07	3.33 (fixed)	-3.03 \pm 0.03
M	174.5/180	1.21 (fixed)	-3.39 \pm 0.05	3.33 (fixed)	-2.86 \pm 0.03
H	188.3/180	1.21 (fixed)	-3.23 \pm 0.04	3.33 (fixed)	-2.85 \pm 0.03
T	211.0/180	1.21 (fixed)	-3.19 (fixed)	3.36 \pm 0.14	-2.92 \pm 0.03
S	229.6/180	1.21 (fixed)	-3.19 (fixed)	3.30 \pm 0.26	-3.13 \pm 0.04
M	174.3/180	1.21 (fixed)	-3.19 (fixed)	3.46 \pm 0.20	-2.90 \pm 0.03
H	195.3/180	1.21 (fixed)	-3.19 (fixed)	3.08 \pm 0.16	-2.76 \pm 0.03

Note. — A is the PSD amplitude in units of Hz^{-1} at the break frequency f_b .

TABLE 3
PSD MODEL FITS USING A SHARPLY-BROKEN POWER-LAW PLUS A LORENTZIAN

Band	χ^2/dof	γ	$\log(f_b(\text{Hz}))$	β	A	$\log(f_L)$	R (%)
T	212.7/178	1.46 (fixed)	-3.60 $^{+0}_{-0.06}$	2.68 \pm 0.10	1.33 \pm 0.03	-3.34 \pm 0.04	3.0 \pm 0.5
S	218.2/178	1.46 (fixed)	-3.60 $^{+0}_{-0.08}$	2.54 \pm 0.14	1.19 \pm 0.04	-3.34 \pm 0.04	<2.0
M	178.1/178	1.46 (fixed)	-3.60 $^{+0}_{-0.06}$	2.70 \pm 0.14	1.35 \pm 0.03	-3.34 \pm 0.04	3.5 $^{+0.5}_{-1.0}$
H	193.7/178	1.46 (fixed)	-3.60 $^{+0}_{-0.06}$	2.42 \pm 0.12	1.38 \pm 0.03	-3.34 \pm 0.04	5.0 \pm 0.5

Note. — Results to fitting the PSDs with a model consisting of a sharply-broken power-law plus a Lorentzian. A is the PSD amplitude in units of Hz^{-1} at the break frequency f_b . The break frequency f_b was constrained to be $10^{-3.60}$ Hz or lower. The low-frequency slope γ was fixed at -1.46. Based on the sum of the χ^2 values for the S, M and H bands, the best-fit value of the Lorentzian centroid frequency f_L was found to be $10^{-3.34\pm0.04}$ Hz; fit parameters above correspond to that value of f_L . In all fits, the quality factor of the Lorentzian Q was assumed to be 5.

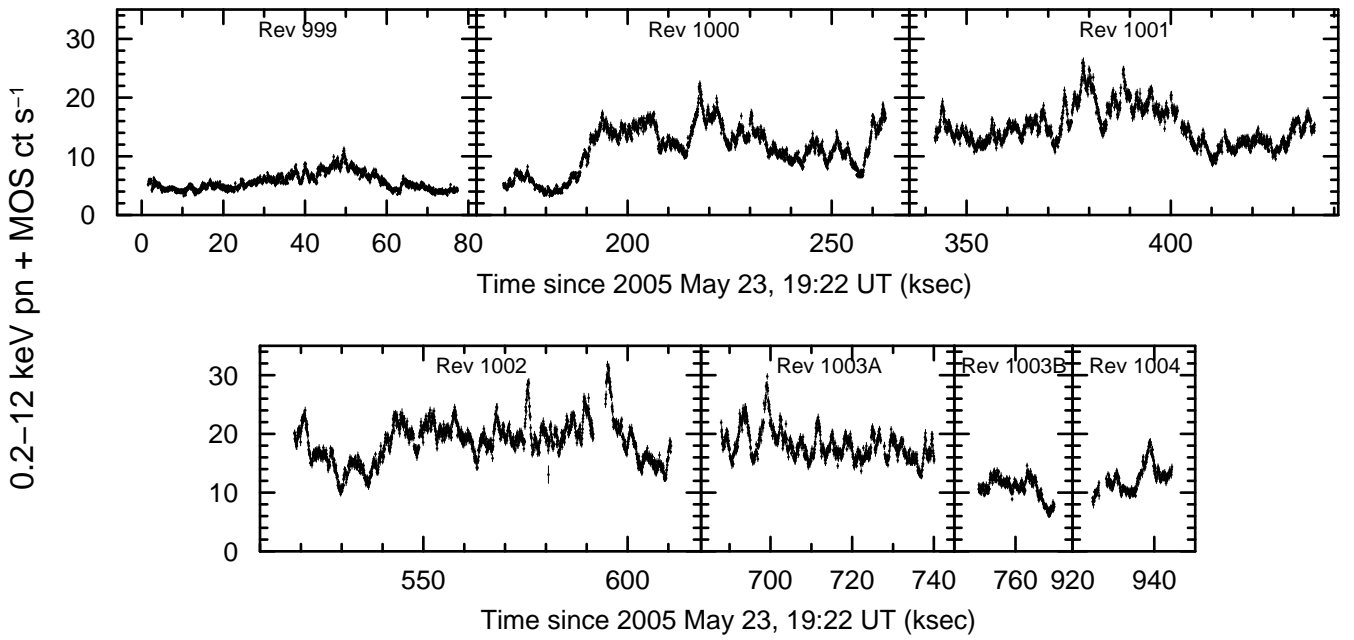


FIG. 1.— 0.2–12 keV EPIC light curves, summed over the pn and MOS cameras, binned to 60 s, for the 2005 observation. All panels have the same scale.

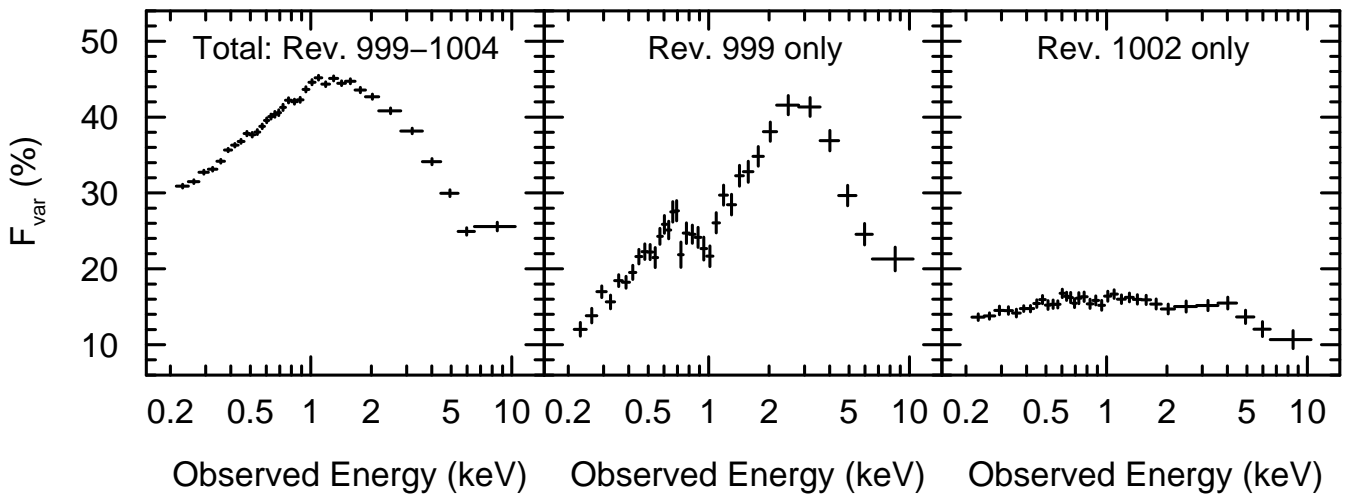


FIG. 2.— F_{var} spectra, constructed using EPIC-pn data, for the entire 2005 observation and for the lowest- and highest-flux revolutions.

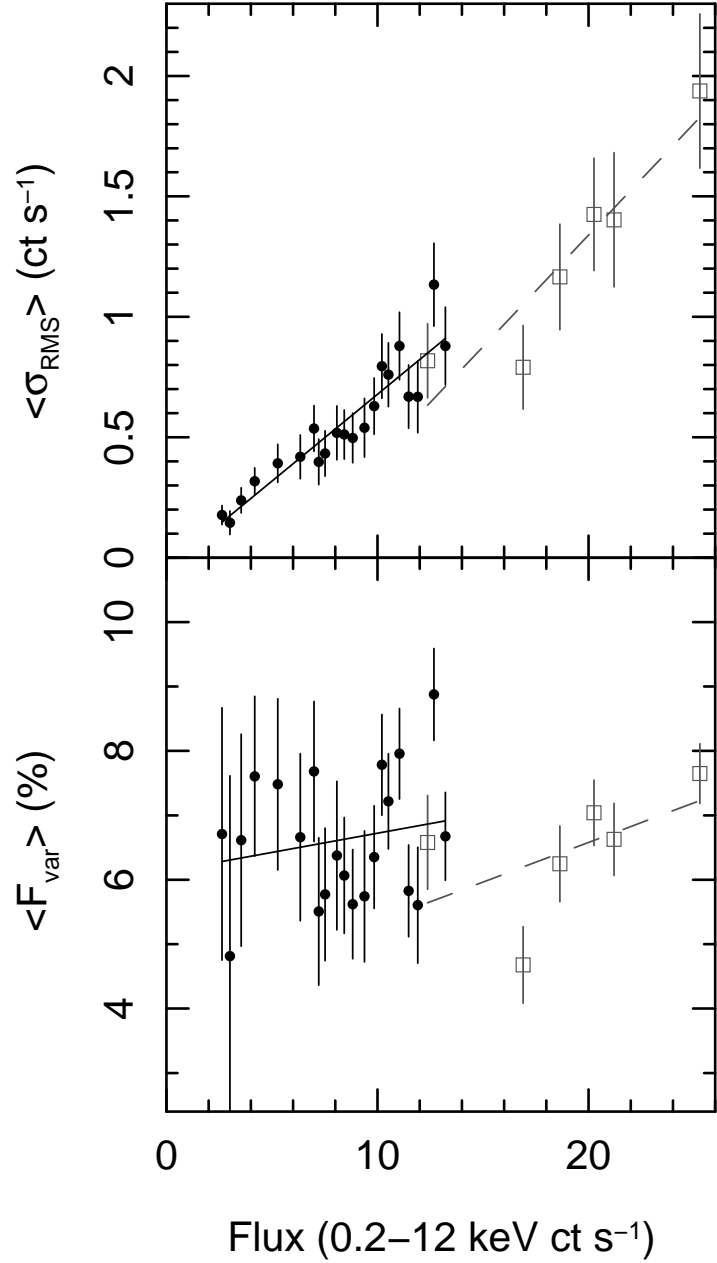


FIG. 3.— The 2005 pn data (black circles) and the 2001 pn data (gray open squares) are both consistent with a linear relation between rms variability amplitude (top) and with constant average fractional variability amplitude $\langle F_{\text{var}} \rangle$. The black solid and gray dashed lines are the best-fit relations for the 2005 and 2001 data, respectively.

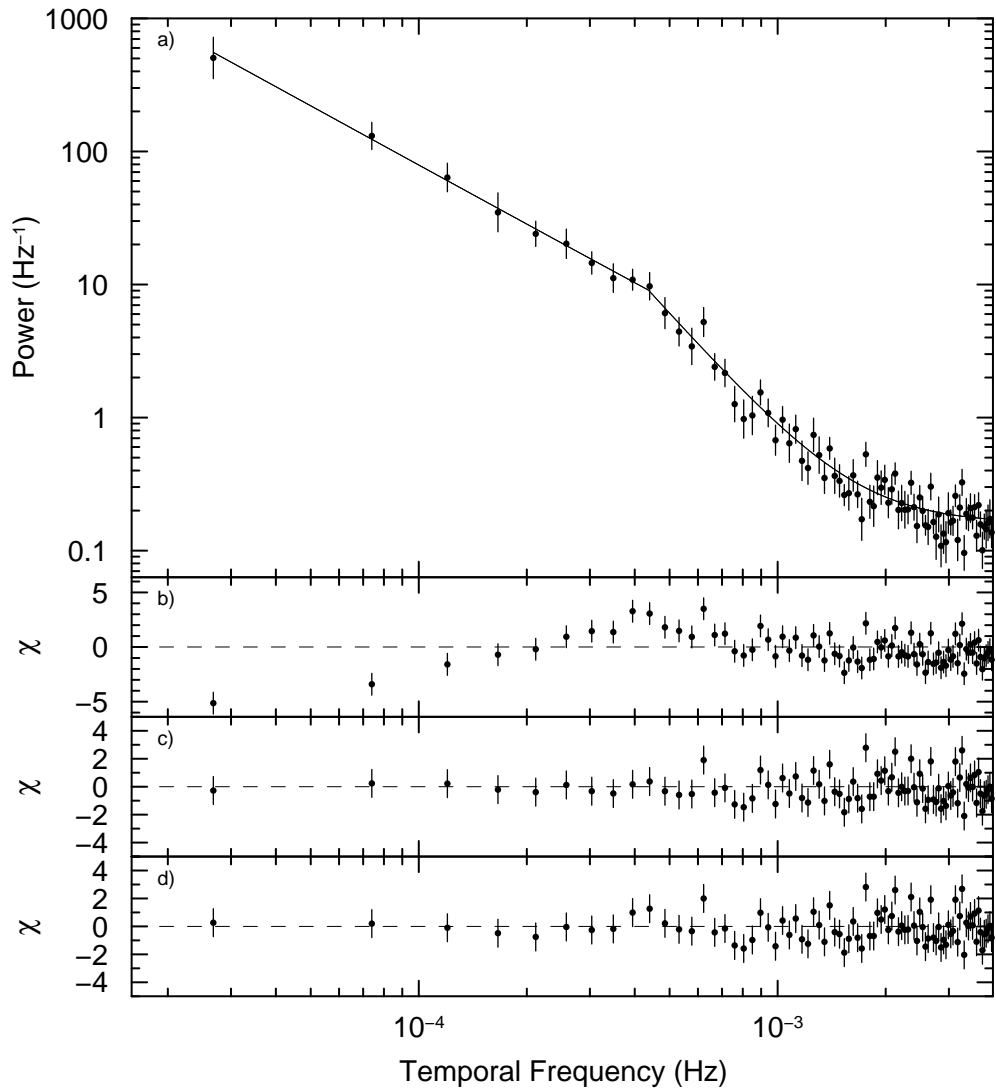


FIG. 4.— *a)* Power density spectrum for the T-band light curve. The solid line denotes the best-fit sharply-broken power-law fit. *b)* Residuals to the best-fit unbroken power-law model; residuals are measured in log space, e.g., based on the logs of the PSD model, data and errors. *c)* Residuals to the best-fit sharply-broken power-law model. *d)* Residuals to the best-fit slowly-bending power-law model. Power due to Poisson noise was included in the models in all panels.

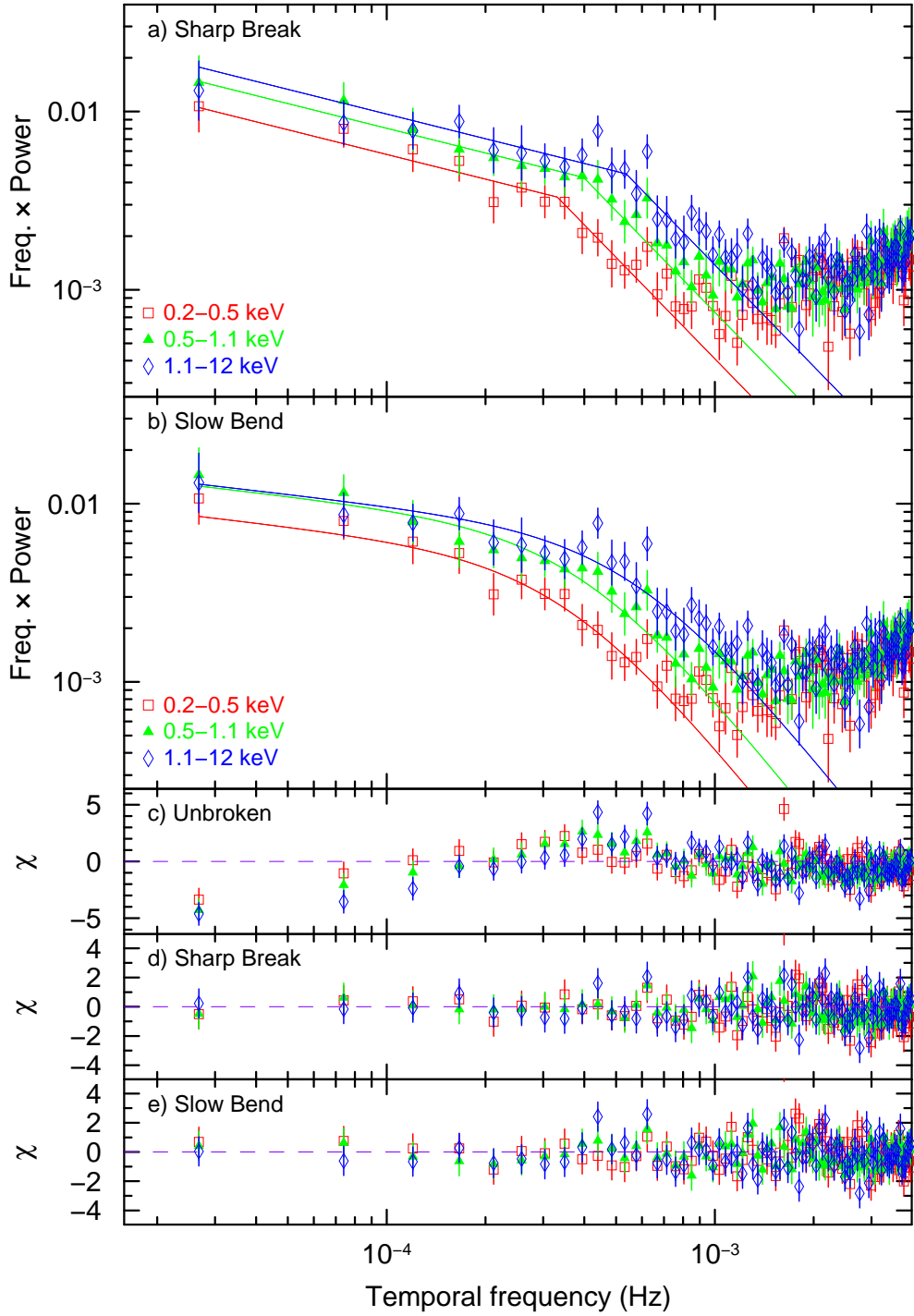


FIG. 5.— *a)* Power density spectra for the S, M, and H-band light curves, plotted in $f - f \times P(f)$ space. The solid lines show the best-fit sharply-broken power-law model assuming the power-law slopes above and below the break β and γ are equal in all bands. The models are plotted with the constant level of power due to Poisson noise omitted for clarity. *b)* Same as *a*), but the solid lines show the best-fit slowly-bending power-law model assuming the power-law slopes above and below the break β and γ are equal in all bands. *c)* Residuals to the best-fit unbroken power-law model. *d)* Residuals to the best-fit sharply-broken power-law model. *e)* Residuals to the best-fit slowly-bending power-law model (power due to Poisson noise was included in the models in panels *b*)–*d*).

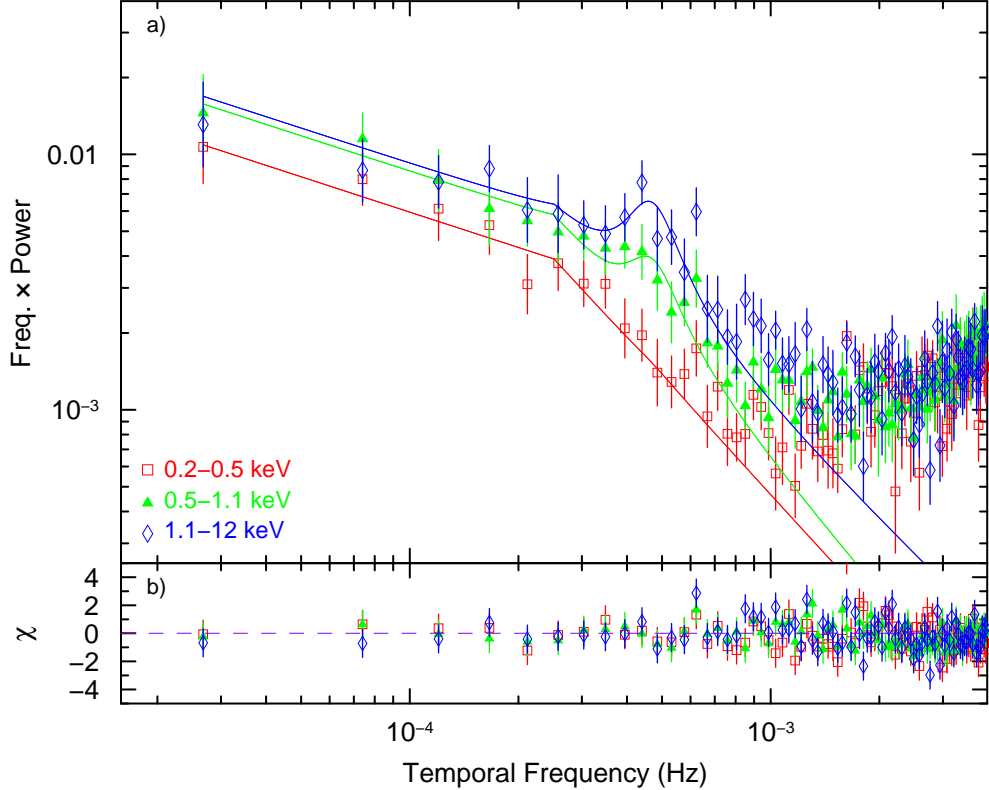


FIG. 6.— a) Power density spectra for the S, M, and H-band light curves, plotted in $f - f \times P(f)$ space. The solid lines show the best-fit model consisting of a sharply-broken power-law, with break frequency constrained to be $10^{-3.60}$ Hz or lower, plus a Lorentzian with a centroid frequency of $10^{-3.32}$ Hz and quality factor $Q = 5$. The models are plotted with the constant level of power due to Poisson noise omitted for clarity. b) Residuals to the best-fit model (with power due to Poisson noise included).

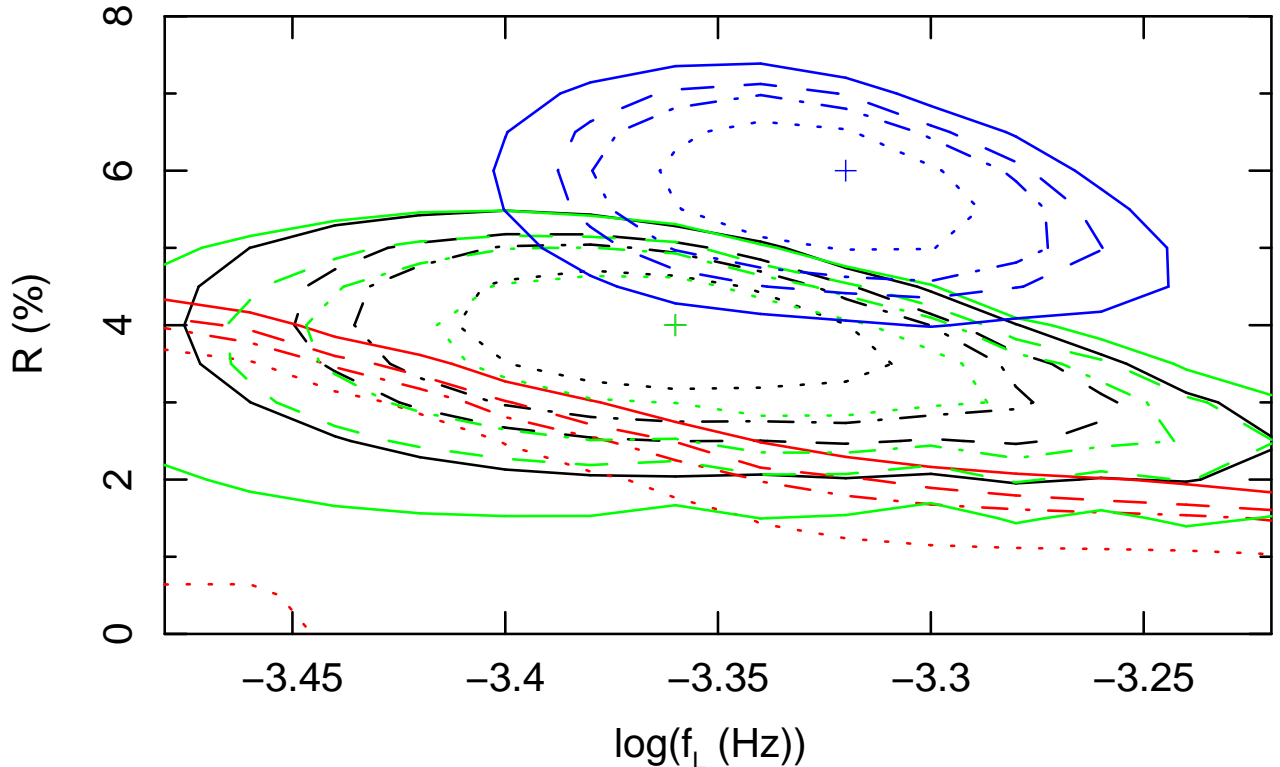


FIG. 7.— Derived confidence contours of the Lorentzian amplitude R versus centroid frequency f_L for each band; black, red, green, and blue denote T, S, M and H bands, respectively. 68, 90, 95 and 99% contour levels are shown (solid, dashed, dash-dotted, and dotted, respectively). The blue cross marks the best-fit value for the H band. The green cross marks the best-fit value for both the M and T bands.

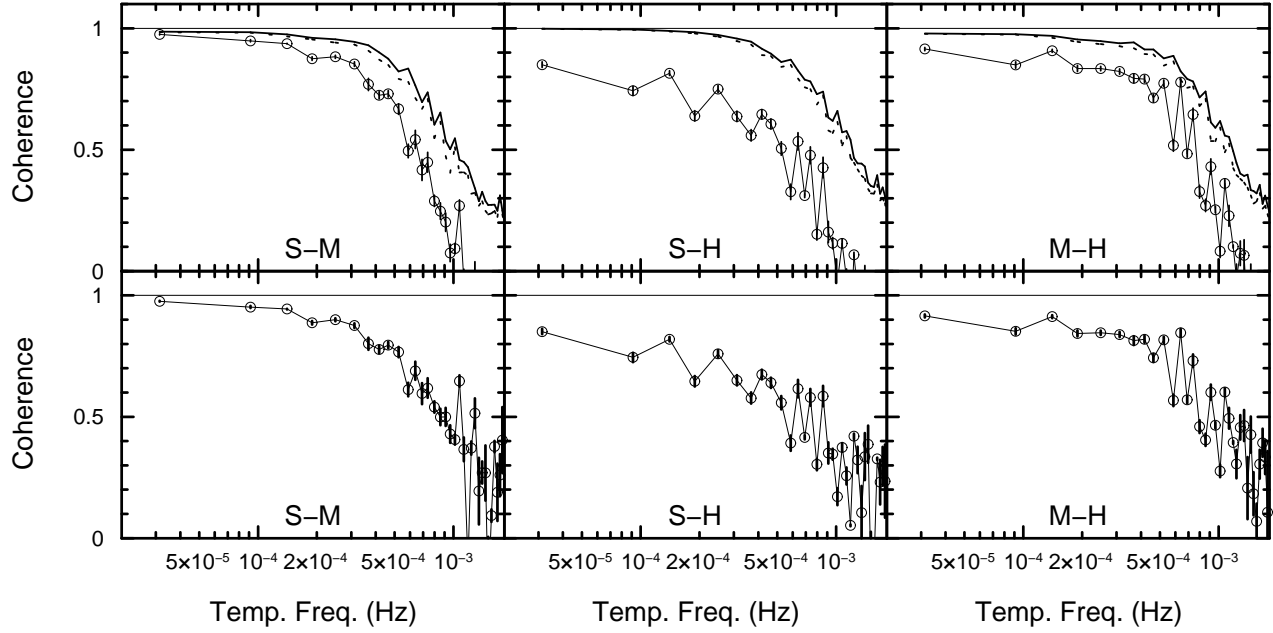


FIG. 8.— The top row shows the observed coherence functions for S–M, S–H and M–H light curve pairs. The thin solid line denotes unity coherence. The dashed and dotted lines denote, respectively, the 90% and 95% confidence limits for spurious lack of coherence due to the combination of Poisson noise and the effect of differing PSD shapes as determined by Monte Carlo simulations. The bottom row shows the estimate of the “intrinsic” coherence (see text for details).

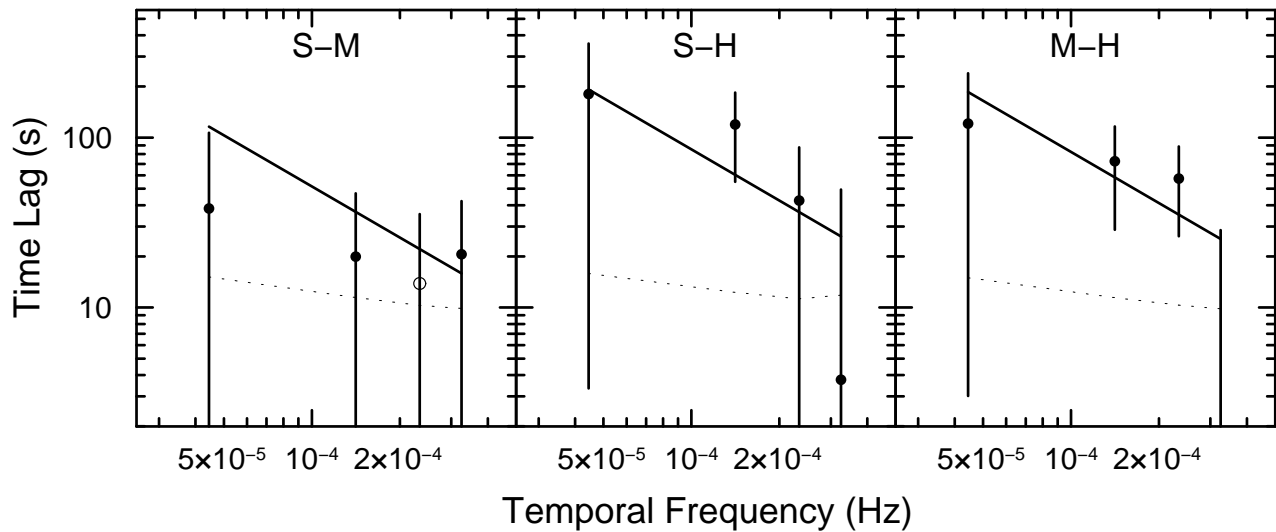


FIG. 9.— Time lag spectra for Mkn 766. Positive lags denote soft band variations leading those in the hard band. A negative lag was detected in the second-highest temporal frequency bin in the S–M time lag spectrum, and its magnitude is denoted by an open circle. The dashed lines denote the sensitivity limits for time lag detection; see text for details. The solid lines denote the best-fit relations to $\tau(f) = Cf^{-1}$.